Diffraction Theory of Optical Interference Moiré and a Device for Production of Variable Virtual Reference Gratings: A Moiré Microscope

by T.W. Shield and K.-S. Kim

ABSTRACT—Optical interference moiré methods are analyzed using Fraunhoffer diffraction theory to relate general large surface deformations to the fringes observed. This analysis determines the Almansi strain in the current configuration from the gradients of the fringe number function. The analysis shows the advantages of an experimental scheme that allows the virtual reference grating to be varied. The ability to vary the virtual reference grating results in a larger dynamic range and the ability to maintain a fringe spacing for maximum accuracy. A moiré microscope has been constructed which has this ability. Digital image processing coupled with optical filtering and phase control is used to enhance the accuracy of the fringe measurements. The variable virtual-reference-grating capability is demonstrated by using it to highlight several aspects of the deformation field near a crack tip in a single crystal of iron-silicon.

Introduction

Applications of moiré methods have been advanced since Foucault[1] first used it for testing lenses and optical systems in 1859. Tolenaar,[2] in 1945, gave a geometrical interpretation of the moiré effect for strain analysis. Morse, Durelli and Sciammarella[3] gave a more complete analysis of geometrical moiré in 1960. Since then geometrical-interference moiré has been explained by many different authors in monographs, for example Theocaris,[4] Durelli and Parks,[5] and in chapters of handbooks, such as Parks[6] and Chiang.[7] An early (1956) treatment of the diffraction aspects of moiré was presented in Guild's monograph.[8] Since the development of laser and microfabrication technologies for the production of fine gratings in the 1970's, optical-interference moiré methods (defined below) are now well established and provide far more sensitivity than conventional geometrical interference moiré. Recently optical interference moiré has also been used and discussed by many others. For example, a description of interference moiré, for small deformations, was presented by Post.[9] McKelvie[10] has discussed the influence of diffraction and aperture size in imaging systems on the accuracy of optical-interference moiré. In the future, nonconventional applications may require geometrical-interference moiré using electron microscopy to provide even higher sensitivity. Even though the mathematical relationship between the fringes and the displacement field is basically the same for both geometrical and optical interference moiré methods, they are fundamentally different from the view point of the optical-image formation system.

Moiré methods can be broken down into two categories: geometrical-interference moiré and optical-interference moiré. The most familiar kind of moiré is geometrical-interference moiré, which can be performed with coarse gratings (or grids). Usually two gratings are employed, one on the specimen and a reference (or interrogation) grating. This method may be analyzed with simple geometrical arguments ignoring the wave nature of light as explained in the next section. In the method of optical-interference moiré, on the other hand, the specimen grating used has a spacing that produces a diffraction angle so large that the imaging system cannot (or is designed not to) collect all of the diffraction orders simultaneously. This method takes advantage of the diffraction phenomena by illuminating the specimen grating with two beams of coherent light and then interfering two of the diffracted beams to produce a fringe pattern. If the two illumination beams are assumed to interfere producing a virtual reference grating which then acts as a reference grating as in the geometrical-moiré method, erroneous analysis will result. The proper analysis uses diffraction theory to derive the relationship between the specimen deformation and the fringes observed. This analysis is presented here. This analysis shows that for a given specimen-grating spacing the sensitivity of the method is determined by which diffraction orders are interfered. The sensitivity of geometrical moiré without fringe multiplication is the lowest sensitivity that is possible using optical-interference moiré. The optical-interference method is $|N-M|$ times as sensitive as the geometrical moiré when Nth order and Mth beams are interfered (usually, one of N and M is negative).

As mentioned earlier, previous descriptions of optical-interference moiré (in Ref. 9 for example) are limited to small deformation kinematics, so that its application was mainly limited to elastic deformations. In this paper, optical-interference moiré is analyzed using large deformation kinematics aimed at applications involving plasticity. The important aspects of plasticity include (1) the deformation is usually large, (2) the stress state is dependent on the loading (or deformation) history, (3) the deformations can be highly inhomogeneous, for example localizations can occur, (4) the rotations of material and the plastic spin are important and can be large. In this paper, a moiré microscope is introduced, which has the capability to measure these types of deformations. To remove the dependence of the linear strains on rigid rotations, the Almansi strains, which are rotationally invariant, are calculated. In addition, a new digital-processing technique coupled with the front-end optical control is introduced

T.W. Shield is Assistant Professor, Department of Aerospace Engineering and Mechanics, University of Minnesota, Minneapolis, MN 55455. K.-S. Kim is Professor, Division of Engineering, Brown University, Providence, RI 02912.

Original manuscript submitted: March 22, 1990. Final manuscript received: February 15, 1991.

to increase the accuracy in determining curves of constant fringe phase. Finally, the moiré microscope is applied to the measurement of plastic-deformation field near the crack tip of an iron-silicon single crystal. Only moiré fringes of the plastic-deformation field are discussed in this paper.

After reviewing the results for geometrical moiré, a mathematical analysis of the fringe formation in optical-interference moiré is presented in the following section. The relationship between the fringes and the surface Almansi strain is given next. The moiré microscope is described and the digital image processing employed is briefly discussed. The advantages of an adjustable virtual reference grating for examination of the deformation field near a crack tip in an iron-silicon single crystal is also shown. Preliminary results for this single crystal have been presented in Ref. 13 and a more complete study appears in a later publication.[11]

Analysis of Optical-interference Moiré Method

To allow comparison between geometrical and optical-interference moiré methods, we will first describe geometrical moiré using the same notation that will later be used for optical-interference moiré. Figure 1 shows how the specimen grid is assigned to material points on the specimen surface in the undeformed configuration and then deforms with the specimen. The deformed grid is imaged through the reference grid to form fringes in the deformed configuration. The fringes are formed in such a way that the fringe-number difference, df, between points P and Q is equal to the difference between the numbers of the specimen and reference grids between these two points. The number of reference grids in the deformed configuration between points P and Q is given by $\mathbf{g} \cdot d\mathbf{x}$. Here $d\mathbf{x}$ is the vector PQ. The number of specimen grids between these two points can be determined from the positions of the points P and Q in the undeformed configuration to be $\mathbf{G} \cdot d\mathbf{X}$. Thus, the fringe-number difference between these points is

$$df = \mathbf{g} \cdot d\mathbf{x} - \mathbf{G} \cdot d\mathbf{X} \tag{1}$$

where $\mathbf{g}$ and $\mathbf{G}$ are the reciprocal grating vectors of the reference and specimen gratings respectively. A reciprodal grating vector, which can be a function of position, has a direction that is perpendicular to the grating lines and has a magnitude equal to the reciprocal of the grating spacing. Equation (1) is the fundamental equation of moiré. Geometrical moiré is based on the fact that if the two grids are in phase then the light transmission is a maximum (bright fringe), and if they are out of phase the transmission is a minimum (dark fringe). Therefore, by taking the difference between the numbers of the two grids between two points, say P and Q in Fig. 1, we can count how many times the two grids are in phase between the two points, which is the number of fringes between these two points. Equation (1) is a mathematical statement of this idea. Grid counting is possible without considering the wave nature (more precisely speaking phase) of light. Methods so described are called 'geometrical moiré'. In real practice, the grid-transmission function, expanded in Fourier series, contains higher harmonics. These harmonics play the same role as the higher diffraction orders in optical-interference moiré and can be used to perform fringe multiplication using optical Fourier filtering or numerical Fourier processing.

Next we will consider optical-interference moiré. This method interferes selected orders of the Fraunhoffer diffraction field[12] of the specimen grating illuminated with coherent light. The electric field representation of light illumination will be expressed as

$$\mathbf{E}(\mathbf{x},t) = \mathbf{A}e^{i\psi(\mathbf{x},t)} \tag{2a}$$

where the phase can be expressed, by integrating the Eikonal equation, $\nabla\psi = \mathbf{k}$,

$$\psi(\mathbf{x},t) = \int_{\mathbf{x}_0}^{\mathbf{x}} \mathbf{k} \cdot d\mathbf{x} - \omega t + \phi_0 \tag{2b}$$

The electric field, $\mathbf{E}$, as a function of the position and time of observation $(\mathbf{x},t)$, has polarization $\mathbf{A}$, wave number $\mathbf{k}$ ($|\mathbf{k}| = 2\pi/\lambda$) and ϕ_0 is the constant phase angle depending on the choice of the reference point $\mathbf{x}_0$. The wavelength and angular frequency of the light are λ and ω respectively. Similarly, the light beam due to diffraction of order N from the surface can be expressed as

$$\tilde{\mathbf{E}}_N = \tilde{\mathbf{A}}_N e^{i\tilde{\psi}_N(\mathbf{x},t)} \tag{3a}$$

where

$$\tilde{\psi}_N(\mathbf{x},t) = \int_{\mathbf{x}_0}^{\mathbf{x}} \tilde{\mathbf{k}}_N \cdot d\mathbf{x} - \omega t + \tilde{\phi}_N \tag{3b}$$

The $\tilde{}$ indicates the diffracted beam. These equations represent general nonplanar waves because $\mathbf{k}$ and $\tilde{\mathbf{k}}_N$ are not constants, they vary from ray to ray. The amplitude also varies from ray to ray. The electric field representations in eqs (2) and (3) should satisfy the wave equation which is a reduced form of the Maxwell equation in a homogeneous medium. This requires that the polarization be harmonic, i.e., $\nabla^2\mathbf{A} = 0$, and guarantees that the intensity flux is divergence free, i.e., $\nabla \cdot \{(\mathbf{A} \cdot \mathbf{A})\mathbf{k}\} = 0$. However, because of the various noise sources in an imaging system, it is desirable to use only the phase information for measuring deformations. A scheme for accurately measuring only the phase contributions by removing the dependence on amplitude is introduced at the end of this section. Therefore, we will only be interested in determining the phase relationships and will not concern ourselves with amplitude or polarization variations.

When a light beam undergoes a transition such as reflection, refraction or diffraction, the phase of the incident wave, ψ is perturbed by $\Delta\psi$. The phase perturbation made by a diffraction grating is $N\Phi(\mathbf{x})$, where $\Phi(\mathbf{x})$

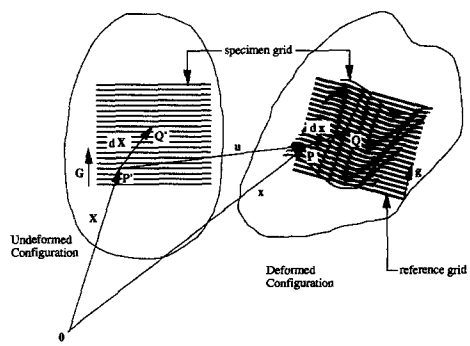

Fig. 1—Geometry for the analysis of geometrical moiré

is the phase of the grating at the point $\mathbf{x}$ and N is the diffraction order (see Appendix A). This provides the relationship

$$\tilde{\psi}_N(\mathbf{x}^*, t) = \psi(\mathbf{x}^*, t) + N\Phi(\mathbf{x}^*) \tag{4}$$

where $\mathbf{x}^*$ denotes the point of diffraction on the deformed specimen grating surface. In terms of the quantities defined above, eq (4) gives the phase, $\tilde{\psi}_N$, of the diffracted beam as

$$\tilde{\psi}_N = \int_{\mathbf{x}_0}^{\mathbf{x}} \tilde{\mathbf{k}}_N \cdot d\mathbf{x} - \omega t + \int_{\mathbf{x}_0}^{\mathbf{x}^*} (\mathbf{k} - \tilde{\mathbf{k}}_N) \cdot d\mathbf{x} + \phi_0 + N\Phi(\mathbf{x}^*) \tag{5}$$

The Fraunhoffer diffraction condition requires that the first-order variation of the phase of the diffracted ray, $\delta\tilde{\psi}_N$, with respect to the spatial variation $\delta\mathbf{X}^*$ vanish (we will only consider the nonrelativistic case here: $\delta t = 0$). Therefore the following equation must hold for arbitrary $\delta\mathbf{X}^*$ on the surface:

$$[\mathbf{k} - \tilde{\mathbf{k}}_N + N\nabla_{x^*}\Phi(\mathbf{x}^*)] \cdot \mathbf{F} \cdot \delta\mathbf{X}^* = 0 \tag{6}$$

where $\mathbf{F}$ is the deformation gradient at $\mathbf{x}^*$ on the surface defined by the relationship $d\mathbf{x}^* = \mathbf{F}d\mathbf{X}^*$. Thus, in order for eq (6) to hold, the quantity in brackets must be proportional to the surface normal $\mathbf{n}$ at $\mathbf{x}^*$. If we denote the wave-number vector of the deformed grating, $\nabla_{x^*}\Phi(\mathbf{x}^*)$, by $\mathbf{k}_g$, then this requirement leads to

$$\tilde{\mathbf{k}}_N = \mathbf{k} + N\mathbf{k}_g + a_N\mathbf{n} \tag{7}$$

where $-a_N$ is the proportionality constant which is determined by the conditions, $|\tilde{\mathbf{k}}_N| = |\mathbf{k}|$ and $\mathbf{k}_g \cdot \mathbf{n} = 0$. These conditions give

$$a_N = -\mathbf{k} \cdot \mathbf{n} \pm [(\mathbf{k} \cdot \mathbf{n})^2 - N\mathbf{k}_g \cdot (N\mathbf{k}_g + 2\mathbf{k})]^{1/2} \tag{8}$$

where the plus sign describes the reflected diffracted ray and the negative sign the transmitted diffracted ray. Equation (7) can be interpreted geometrically as shown in Fig. 2. Because the vectors $\mathbf{k}$ and $\tilde{\mathbf{k}}_N$ must have the same length, if they are drawn originating at the same point their ends must lie on the same circle. The difference between these two vectors in the tangent plane of the surface is $N\mathbf{k}_g$. This determines the end point for $\tilde{\mathbf{k}}_N$ on the circle. Using this construction the value of a_N can then be directly read off the figure as the magnitude of the normal component of the difference between $\mathbf{k}$ and $\tilde{\mathbf{k}}_N$ which agrees with eq (8).

In optical-interference moiré, the diffracted rays $\tilde{\mathbf{k}}_N^{(1)}$ and $\tilde{\mathbf{k}}_N^{(2)}$ of two different incident rays $\mathbf{k}^{(1)}$ and $\mathbf{k}^{(2)}$ are collected with a converging lens and interfered on the image plane to produce fringes. In order that only the desired diffraction orders of the two incident rays reach the image plane, an aperture is used to filter the light passing through the focal plane of the lens. If ξ is a unit vector along the axis of this lens and $\mathbf{x}'$ is the position vector from the axis in the focal plane, the diffracted ray $\tilde{\mathbf{k}}_N$ intersects the focal plane at $\mathbf{x}'_N$,

$$\mathbf{x}'_N = l_f \left\{ \frac{(\mathbf{k} + N\mathbf{k}_g + a_N\mathbf{n})}{(\mathbf{k} + N\mathbf{k}_g + a_N\mathbf{n}) \cdot \xi} - \xi \right\} \tag{9}$$

where l_f is the focal length of the lens. Thus the diffracted rays of different orders intersect the focal plane at different points. This allows an aperture on the focal plane to be used to select the orders of the rays that reach the image plane. If η is used to denote the gradient of the grating phase function in the reference configuration,

$$\eta = 2\pi\hat{\mathbf{G}}^* = \nabla_{X^*}\Phi = \mathbf{F}^T \cdot \mathbf{k}_g \tag{10}$$

where $\hat{\mathbf{G}}^*$ is the reciprocal specimen grating vector, we can write

$$\mathbf{k}_g = (\mathbf{F}^T)^{-1} \cdot \eta \tag{11}$$

Replacing $\mathbf{k}_g$'s in eqs (8) and (9) using eq (11), eq (9) provides a complete description of the focal-plane mapping of the diffracted rays as a function of deformation gradient. This is the fundamental equation of the Fourier filtering of the optical-interference moiré.

If we assume that the in-plane strain, ϵ, and in-plane rotation, ω, are small then eqs (7), (11) and (9) for the case of $\xi = \mathbf{n}$ give

$$\mathbf{x}'_N = \frac{l_f}{\tilde{\mathbf{k}}_N \cdot \mathbf{n}} [N(\omega - \epsilon) \cdot \eta + a_N\delta\mathbf{n}] + \mathbf{x}'^{(0)}_N \tag{12}$$

where

$$\mathbf{x}'^{(0)}_N = l_f \left[\frac{\mathbf{k} - (\mathbf{k} \cdot \mathbf{n})\mathbf{n} + N\eta}{[(\mathbf{k} \cdot \mathbf{n})^2 - N^2|\eta|^2 - 2N\eta \cdot \mathbf{k}]^{1/2}} \right] \tag{13}$$

and $\delta\mathbf{n}$ is the change in the surface normal.

After the desired orders are filtered on the focal plane, they pass on to the image plane to form the fringe pattern. The intensity function for the resulting fringe pattern, if mapped virtually back to the specimen surface, is given by

$$I(\mathbf{x}^*) = |\tilde{\mathbf{E}}_N^{(1)} + \tilde{\mathbf{E}}_M^{(2)}|^2 = \tilde{I}_N^{(1)} + \tilde{I}_M^{(2)} + 2\tilde{\mathbf{A}}_N^{(1)} \cdot \tilde{\mathbf{A}}_M^{(2)} \cos\Psi \tag{14}$$

where $\Psi = \tilde{\psi}_N^{(1)} - \tilde{\psi}_M^{(2)}$ is the phase difference between $\tilde{\mathbf{E}}_N^{(1)}$ and $\tilde{\mathbf{E}}_M^{(2)}$. This can be obtained from eq (5) as, choosing $\mathbf{x}_0$ on the specimen surface,

$$\Psi(\mathbf{x}^*) = \int_{\mathbf{x}_0^*}^{\mathbf{x}^*} (\mathbf{k}^{(1)} - \mathbf{k}^{(2)}) \cdot d\mathbf{x} + (N - M)\Phi(\mathbf{x}^*) + \phi_0^{(1)} - \phi_0^{(2)} \tag{15}$$

In eq (14) the oscillating term, $\cos\Psi$, is the moiré fringe, thus the fringe number f is given by

$$f = \frac{\Psi}{2\pi} = \int_{\mathbf{x}_0^*}^{\mathbf{x}^*} \mathbf{g} \cdot d\mathbf{x} - (M - N)\frac{\Phi}{2\pi} + f_0 \tag{16}$$

The reciprocal grating vector of the virtual reference grating, $\mathbf{g}$, is given by

$$\mathbf{g} = (\mathbf{k}^{(1)} - \mathbf{k}^{(2)})/(2\pi) \tag{17}$$

The constant term in eq (16), f_0, is the difference $(\phi_0^{(1)} - \phi_0^{(2)}/(2\pi)$. The sign convention of the diffraction orders M and N is chosen in such a way that $M - N > 0$. Using the definition of $\hat{\mathbf{G}}^*$ in eq (10), eq (16) can be written

$$df = \mathbf{g} \cdot d\mathbf{x}^* - (M - N)\hat{\mathbf{G}}^* \cdot d\mathbf{X}^* \tag{18}$$

This equation has the same form as eq (1) for geometrical moiré and can be made identical if the definitions of virtual reference grating spacing and effective specimen grating spacing, as defined in the next paragraph, are used.

The virtual reference grating has the spacing caused by the optical interference resulting from the intersection of the two illumination beams, each with an angle θ to the optical axis. The resulting virtual reference spacing is given by

$$d^{vr} \equiv \frac{1}{|\mathbf{g}|} = \frac{\lambda}{2 \sin \theta} \tag{19}$$

The virtual reference grating then produces fringes by interfering with the effective specimen grating. The effective specimen grating is determined by the specimen grating, $\hat{\mathbf{G}}^*$, and the orders of the diffracted beams that are interfered to form the moiré fringes. The effective specimen grating spacing, D^{es}, is related to the actual specimen grating spacing, D, by

$$D^{es} \equiv \frac{1}{|\mathbf{G}^*|} = \frac{D}{M-N} \tag{20}$$

where M and N are the orders of the diffracted beams which are interfered and $\mathbf{G}^* = (M-N)\hat{\mathbf{G}}^*$. The factor $M-N$ is the sensitivity increase over geometrical moiré. If these values of the grating spacings are used, then the determination of the displacements and strains from the fringe patterns can proceed identically for both geometrical and optical-interference moiré in the next section.

In the analysis of the fringe patterns above, the illumination of the incident beams is not uniform, in general, and the efficiencies of the gratings on the specimen vary with position. Both of these quantities vary slowly (relative to the fringe spacing) with position and contain noise. In order to use a single-level binarization method to determine lines of constant phase, it is necessary to remove these variations from the fringe pattern. A simple way to accomplish this is through control of the relative phase of the two incident beams.

The relative phase of the two beams is $2\pi f_0 = \phi_0^{(1)} - \phi_0^{(2)}$. Examination of eq (16) shows that changing f_0 directly changes the phase of the fringes. If we can produce two fringe patterns, one with $f_0 = 0$ and the other with $2\pi f_0 = \phi_s$, then the difference of the two fringe patterns will not involve the intensities of the diffracted (or incident) beams. For the first choice of f_0 we can write

$$I_1(\mathbf{x}^*) = \tilde{I}_N^{(1)} + \tilde{I}_M^{(2)} + 2\tilde{\mathbf{A}}_N^{(1)} \cdot \tilde{\mathbf{A}}_M^{(2)} \cos \Psi \tag{21}$$

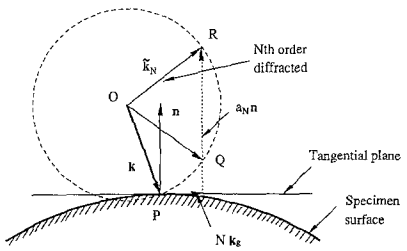

Fig. 2—Geometrical interpretation of diffraction from a grating on a surface

and for $2\pi f_0 = \phi_s$, we have

$$I_2(\mathbf{x}^*) = \tilde{I}_N^{(1)} + \tilde{I}_M^{(2)} + 2\tilde{\mathbf{A}}_N^{(1)} \cdot \tilde{\mathbf{A}}_M^{(2)} \cos (\Psi + \phi_s) \tag{22}$$

The difference intensity is then

$$I_1(\mathbf{x}^*) - I_2(\mathbf{x}^*) = 4\tilde{\mathbf{A}}_N^{(1)} \cdot \tilde{\mathbf{A}}_M^{(2)} \sin (\phi_s/2) \sin (\Psi + \phi_s/2) \tag{23}$$

which does not involve the intensities of the diffracted (or incident) beams other than as a coefficient of the oscillatory term. If we binarize this with a threshold of zero to determine the curves along which the fringe phase is equal to $n\pi - \phi_s/2$, n = integer, then the coefficient of $\sin (\Psi + \phi_s/2)$ does not enter the results. This is because we are determining the curves along which $\sin (\Psi + \phi_s/2) = 0$. The constant factor of $\sin \phi_s/2$ determines the contrast of the difference fringes. The greatest contrast occurs for a phase difference of π. Because the strains only involve the gradients of the fringe number function, f, and ϕ_s is a constant, the values of the strains found are independent of the value of ϕ_s. Thus, this method is insensitive to errors in ϕ_s and it can simply be chosen to maximize the contrast. This results in an effective fringe multiplication factor of two, which is a direct increase in the sensitivity of the method.

This process also allows the level for binarization to be determined exactly. With this technique the binarization threshold is always exactly zero. If a difference fringe image was not used, the average illumination level would have to be used. This could lead to errors in determining the curves of constant phase. The subtraction process also eliminates much of the noise introduced into the fringe pattern by sources of noise that affects the intensities of the illumination beams.

Deformation Analysis with Moiré Methods

In the previous section, the equations relating the fringe number to the surface position in the deformed configuration have been derived for both moiré methods. Examination of eqs (1) and (18) shows that both geometrical and optical-interference moiré methods are described by an equation of the same form. This equation is

$$df = \mathbf{P} \cdot \mathbf{g} \cdot d\mathbf{x} - \mathbf{G} \cdot d\mathbf{X} \tag{24}$$

where the position vector $\mathbf{X}$ locates the surface material point in the undeformed configuration, which is located at $\mathbf{x}$ in the deformed (current) configuration. The projection tensor, $\mathbf{P}$, is related to the normal to the surface, $\mathbf{n}$, through

$$\mathbf{P} = \mathbf{I} - \mathbf{n} \otimes \mathbf{n} \tag{25}$$

where $\mathbf{I}$ is the intensity tensor and $\otimes$ indicates tensor product. Equation (24) holds with and without $\mathbf{P}$. However, we have introduced the projection tensor into eq (24) to map the virtual reference grating onto the surface of the specimen. By doing this the quantities $(\mathbf{P} \cdot \mathbf{g})$, $\mathbf{x}$, $\mathbf{G}$ and $\mathbf{X}$ are all measured in the specimen surface coordinates. In the notation of the last section they would have been starred. For simplicity in this section the stars are omitted.

If linear gratings are used for the specimen and interrogation gratings, $\mathbf{g}$ and $\mathbf{G}$ are constant vectors. This allows eq (24) to be integrated to give

$$f - f_0 = \mathbf{g} \cdot \mathbf{x} - \mathbf{G} \cdot \mathbf{X} \tag{26}$$

Introducing the displacement vector $\mathbf{u}$, defined by

$$\mathbf{u} = \mathbf{x} - \mathbf{X} \tag{27}$$

eq (26) can be rewritten as

$$\mathbf{G} \cdot \mathbf{u} = (f - f_0) - (\mathbf{g} - \mathbf{G}) \cdot \mathbf{x} \tag{28}$$

Equation (28) shows that two independent $\mathbf{G}$ vectors (and $\mathbf{g}$ vectors) are required to measure the two in-plane displacement components on the object plane. The last term in eq (28) represents the carrier frequency of the fringe pattern. In many applications, $\mathbf{g}$ is set equal to $\mathbf{G}$ nullifying the carrier frequency of the fringe pattern.

If we again consider eq (24) for the general case, we can rewrite it as

$$(\mathbf{F}^{-1})^T \cdot \mathbf{G} = \mathbf{P} \cdot (\mathbf{g} - \nabla f) \tag{29}$$

where $\mathbf{F}$ is the surface-deformation gradient tensor. The projection tensor has appeared again because the gradient of f is taken in the object plane and then projected onto the specimen surface. To completely determine the surface strain field, two specimen gratings $\mathbf{G}^1$ and $\mathbf{G}^2$ must be used, together with the information on the out of plane displacement. A compact representation of the surface strains can be found if we first form the second-order specimen-grating tensor Γ, as

$$\Gamma = \sum_{\alpha=1}^{2} \mathbf{G}^\alpha \otimes \mathbf{G}^\alpha \tag{30}$$

For each specimen grating $\mathbf{G}^\alpha$, a different interrogation grating $\mathbf{g}^\alpha$ is used to produce a fringe pattern f^α. Equation (29) holds for each choice of α with $\mathbf{G}$, $\mathbf{g}$ and f replaced by $\mathbf{G}^\alpha$, $\mathbf{g}^\alpha$ and f^α, but the deformation gradient is the same in both cases. By taking the tensor product of both sides of eq (29) with $\mathbf{G}^\alpha$ for both values of α and adding the results, we find

$$(\mathbf{F}^{-1})^T = \mathbf{H} \cdot \Gamma^{-1} \tag{31}$$

where

$$\mathbf{H} = \sum_{\alpha=1}^{2} \mathbf{P} \cdot (\mathbf{g}^\alpha - \nabla f^\alpha) \otimes \mathbf{G}^\alpha \tag{32}$$

Then the inverse of the finger deformation tensor becomes

$$(\mathbf{F} \cdot \mathbf{F}^T)^{-1} = \mathbf{H} \cdot \Gamma^{-1} \cdot (\Gamma^{-1})^T \cdot \mathbf{H}^T \tag{33}$$

and this provides a finite strain measure (Almansi strain) in the deformed configuration. Because we have the complete information of the displacement field, we could determine the other finite strain measures such as Green strain in the undeformed configuration. However, because we can only view the deformed configuration in experiments, the Almansi strain is a more useful measure. The Almansi strain is defined to be

$$\mathbf{E}^A = \tfrac{1}{2}[\mathbf{I} - (\mathbf{F} \cdot \mathbf{F}^T)^{-1}] \tag{34}$$

If we use a pair of linear specimen gratings of pitch D that are orthogonal, then Γ becomes

$$\Gamma = \frac{1}{(D^{es})^2}\mathbf{I} \tag{35}$$

where D^{es} is related to D through eq (20). In this case, eq (33) reduces to

$$(\mathbf{F} \cdot \mathbf{F}^T)^{-1} = (D^{es})^2 \sum_{\alpha=1}^{2} \mathbf{P} \cdot (\mathbf{g}^\alpha - \nabla f^\alpha) \otimes (\mathbf{g}^\alpha - \nabla f^\alpha) \cdot \mathbf{P}^T \tag{36}$$

thus we have

$$\mathbf{E}^A = \frac{1}{2}\left[\mathbf{I} - (D^{es})^2 \sum_{\alpha=1}^{2} \mathbf{P} \cdot (\mathbf{g}^\alpha - \nabla f^\alpha) \otimes (\mathbf{g}^\alpha - \nabla f^\alpha) \cdot \mathbf{P}^T\right] \tag{37}$$

As shown in eqs (30)-(34), the Almansi strain measure depends, in general, on the direction of the undeformed specimen grating, $\mathbf{G}$. However, if the specimen gratings are orthogonal in the undeformed configuration, the strain measure is not dependent on the direction of $\mathbf{G}$, as shown by eq (37). This indicates that if in practice orthogonal specimen gratings are produced, it is not necessary to record their initial directions. Only their spacing need be known. This is simply another way of noting that the Almansi strain is rotationally invariant. Therefore, unlike the linear strain measure, calculating the Almansi strains does not introduce any errors caused by the rigid-body motion of the specimen.

Equation (37) shows that the observed strain is the projection of the surface strain onto the object plane. If the deformed specimen surface and the object plane of the imaging system are not aligned, the projection must be taken into consideration. However, if the misalignment is small, the difference between the surface strain and the observed strain is second order. If it is necessary to include this correction, then the projection tensor can be constructed for the surface by measuring the slope of the surface using image shearing interferometry.[11]

For the usual case of $|\mathbf{P} \cdot \mathbf{g}| = |\mathbf{G}| = 1/D^{es}$ and orthogonal ($\mathbf{P} \cdot \mathbf{g}^{(1)}$, $\mathbf{P} \cdot \mathbf{g}^{(2)}$), this becomes

$$\mathbf{E}^A = (D^{es})^2 \mathbf{P} \cdot \left\{\text{sym}\left[\sum_{\alpha=1}^{2} \mathbf{g}^\beta \otimes \nabla f^\alpha\right] - \frac{1}{2}\sum_{\alpha=1}^{2} \nabla f^\alpha \otimes \nabla f^\alpha\right\} \cdot \mathbf{P}^T \tag{38}$$

where sym [ ] denotes the symmetric part of a second-order tensor. If the strains are assumed to be small, the second term is of second order. The projection is the identity if the changes in the surface normal are also small and initially $\mathbf{g}$ was parallel to a planar specimen surface. Under these conditions, the linear strain ϵ is given by

$$\epsilon = (D^{es})^2 \,\text{sym}\left[\sum_{\alpha=1}^{2} \mathbf{g}^\alpha \otimes \nabla f^\alpha\right] \tag{39}$$

Even for small strain problems this is not a good strain measure to use in practice. The strains given by eq (39) depend on the rigid-body rotations which appear as fictitious shear strains. To avoid this problem the specimen has to be carefully aligned. If it is not, this dependence leads to large errors in the measured strain. This required alignment imposes unnecessary restrictions on the experimental setup, complicating, for instance, real-time

measurements and other useful developments of the method. Therefore, it is advisable to use eq (37), even for small strain measurements.

As shown in eq (31), the deformation gradient, **F**, can be measured using moiré methods. Thus, the local rotation, **R**, and the pure deformation, **U**, can also be determined from $\mathbf{F} = \mathbf{R} \cdot \mathbf{U}$. Various local rotation measures, such as continuum, crystal and plastic rotations (or spins) are important in micromechanics of solids. Calculation of these rotation measures is beyond the scope of this paper and will appear elsewhere.[11]

The Microscope Apparatus

The microscope described here illuminates the specimen with two beams of coherent light to produce fringes. Previous methods have employed a mirror to reflect half of a beam onto its other half, but this makes adjustment of the system difficult. In order to allow a variable virtual reference grating and high magnification, a more versatile optical system was developed. The microscope employs a beam splitter in the optical path of the imaging system to allow through-the-lens illumination of the specimen with the virtual reference grating. The two beams directed into this splitter are adjustable in spacing and orientation around an axis centered between the two beams and parallel to them. This allows a virtual reference grating to be produced with a range of spacings and any orientation. A schematic of this system is shown in Fig. 3.

The He-Ne laser [at (a) in Fig. 3] produces a beam which is expanded, spatially filtered and collimated by the two lenses and a pinhole at (b). A beam steerer (c) allows the beam to be accurately aligned along the axis of the assembly of parts (d)-(f). This is necessary because of the rotation of the first beam splitter assembly [(e) and (f)] about this axis. The lens at (d) is chosen and placed to produce a collimated beam exiting from the objective lens (h). The incoming laser beam is offset from the system axis by the glass plate (e). It is this offset that controls the virtual reference grating spacing. The beam splitter (f) produces two beams whose spacing is related to the tilt of the glass plate (e). These two components can be rotated about their center line to rotate the reference grating orientation. After partial reflection in the second beam splitter (g), these two beams are focused by the objective lens (h) and cross at its focal plane. Since the diameter of these beams is finite, the volume of virtual grating produced includes the specimen (i), which is at a distance from the objective lens slightly greater than its focal length. Not shown is the wedge used to vary the phase of one of the illumination beams. This is inserted between elements (f) and (g) of the microscope. This point is at the focal point of lens (d) and thus the wedge produces a uniform phase change across the whole beam.

The remaining system elements make up the imaging system, which selects and interferes the desired diffraction beams. The iris (j) is located at the focal plane of the objective lens (h) and is used to pick out the diffraction beams to be combined into a fringe pattern on the camera screen (k). Both the diameter of the iris opening and its location need to be adjustable to allow the best quality fringe pattern to be produced with the desired diffracted beams as outlined in 'Analysis of Optical-interference Moiré Method' above. The television camera is connected to a frame grabber installed in a microcomputer, as well as a monitor and VCR for real-time data storage and later review of test results. The frame grabber allows the images of the fringe patterns to be stored and manipulated digitally on the computer. These digital images can also be directly printed on a laser printer. The digital data-reduction procedures will be discussed in the next section.

In a previous publication,[13] we calculated a theoretical calibration curve and compared it to measured results using a grating of known spacing. Very good agreement was found between the predictions and the experimental findings.

Digital Data Processing

In the previous section we have already mentioned that the output of the video camera is connected to a frame grabber which allows the images to be stored and manipulated digitally on a computer. The frame grabber stores each video frame as a 512 × 480 array of 256 grey levels for a total storage requirement of approximately 256 kilobytes per frame. The large amounts of data involved make any image processing undertaken computationally expensive. At this stage in the system development, only schemes simple enough to run in a reasonable amount of time on a personal computer have been implemented. Only the fringe locations are used at this stage so the fringes can be reduced to simple white and black patterns. Thus the first attempt at fringe data reduction is to reduce the fringe patterns to two level images through binarization. Once a binary image is obtained it is straightforward to detect the fringe edges and store the data as line segments which can then be used to determine the fractional fringe number on a regularly spaced grid of points. The displacements and strains can then be calculated at these evenly spaced points. The details of these calculations will be presented in Ref. 11. Here we will only present the images at each step in the process. The specimen is described in Appendix B.

Figures 4 and 5 are the original fringe images that differ in phase by π. These two images can be subtracted to remove most of the background noise from the fringes and accurately determine the binarization level as discussed above. The difference image is shown in Fig. 6. A binarization process is then applied to Fig. 6 to give Fig. 7(a). Figure 7(b) shows the result of binarizing one of the original fringe images at its average illumination level. The added noise in this figure as well as the clearly inaccurate location of the lines of constant phase show the importance of using the subtraction process. A smoothing algorithm is then used to remove the 'salt and pepper' noise from the binary image in Fig. 7(a). This final image is shown in Fig. 8. A semi-automatic edge tracing routine is then used to trace the edges of the fringes which are curves of constant phase. These data are then stored as (x, y) points on the curves shown in Fig. 9. Determination of

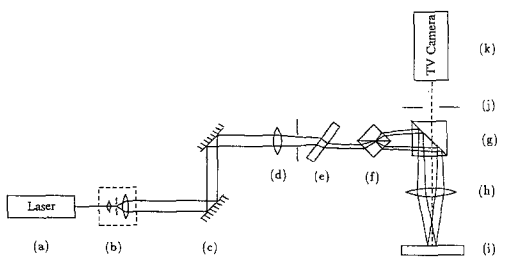

Fig. 3—Schematic of the microscope

the displacement and its gradient then can proceed using these data.

Characteristic Results

With coarse gratings the basic diffraction angle is relatively small, and this small angle results in a narrow strain dynamic range. Since the Fourier filtering aperture must also be relatively small, this results in large sensitivity to surface tilt which appears as a horizontal dead spot (no fringes) emanating from the notch tip in Fig. 10(a). Ordinary optical microscopy shows that the dead spot is located at the place where the local surface tilt is large. In this paper we only present the moiré fringes associated with the horizontal displacement component, the crack-opening direction. Figure 10(a) shows the moire fringes around the crack tip formed with virtual reference grating, **g**, chosen to display the fringe kinks, which indicate jumps in strain. The fringes do not show, at our current resolution, any fringe steps which would indicate jumps in displacement. However, closer examination of the fringe kinks shows that the strains change from one state of strain to another across a very narrow band. Two of the three sectors in Fig. 10(a) also appear to have parallel and equally spaced fringes. This indicates that the extensional strain in horizontal direction is constant in these sectors. Figures 10(b) and 10(c) show the fringe patterns when we adjust **g** to null out the fringes in each

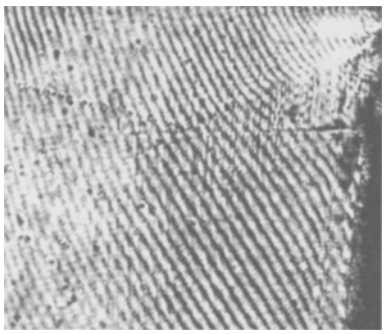

Fig. 4—An original fringe image

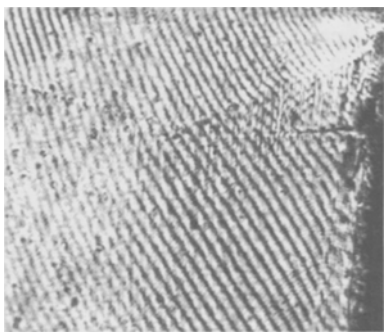

Fig. 5—A fringe image whose phase differs by π from the fringes in Fig. 4

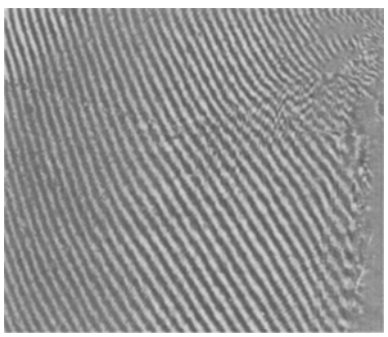

Fig. 6—The difference between Figs. 4 and 5

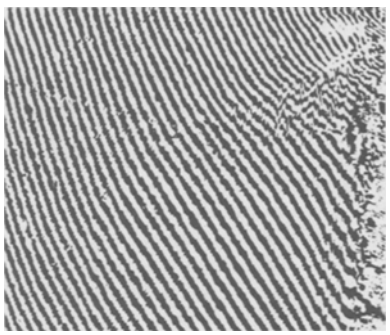

Fig. 7(a)—Binarization of fringes in Fig. 6

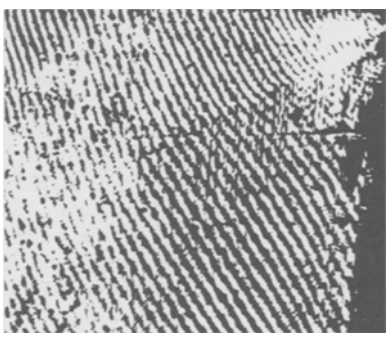

Fig. 7(b)—Binarization of fringes in Fig. 4

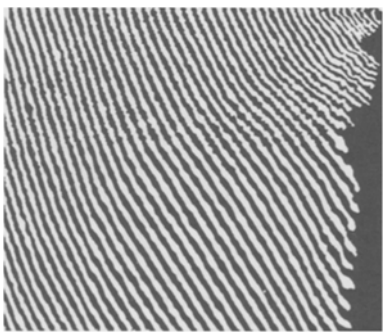

Fig. 8—Smoothed version of the fringes in Fig. 7(a)

of these sectors. The constant strain regions extend from the crack tip to the point at which the far field variations due to the external boundaries become large. This is noticeable in Fig. 10(c) as the widely spaced fringes at the upper right in the nulled sector.

Conclusion and Future Work

An initial version of a moiré microscope has been introduced. The device uses optical interference moiré and has the capability of controlling the pitch and the direction of the virtual reference grating. This allows a fringe pattern to be produced that is optimal for analysis. By subtracting fringe patterns whose phases differed by π, a large amount of noise was removed and the constant phase lines were determined accurately. This process is required because of the large amounts of noise always present in greatly magnified moiré fringes.

Comprehensive analyses of optical interference moiré and the associated fringes have been presented. This analysis shows that the orthogonality of the checkered specimen grating greatly simplifies the fringe analysis. The effective accuracy of the specimen grating and the controllability of the virtual reference grating are the most important factors highlighted by the analysis. In addition, fringe analysis using digital image processing also improves the utility of the system.

The microscope has been successfully used to study the deformation field near a crack tip in an iron-silicon single crystal. This is a demonstration of the applicability of the microscope to highly inhomogeneous large deformations. Many interesting features of anisotropic plasticity of near crack-tip deformation have been observed and a future publication[11] will elaborate on the results given in Ref. 13.

Acknowledgment

Support for this research was provided by the Office of Naval Research contract number ONR N00014-90-J-1295. We would like to thank Professor J.R. Rice of Harvard University for his support for the second author during his sabbatical visit at Harvard University and for providing the motivation to examine single-crystal plasticity. We also appreciate T. Wei of Brown University for making the gratings and R. Nikolic of Harvard University for providing the notched single-crystal specimen.

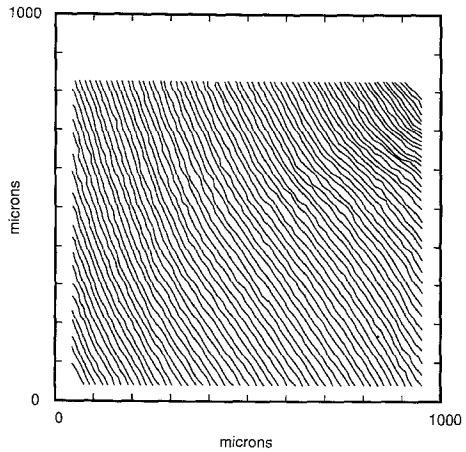

Fig. 9—Traces of the fringe edges in Fig. 8

References

1. *Foucault, L., Annls. Obs. Paris,* **5**, *197 (1859).*
2. *Tolenaar, D., Interferentieverschijnselen bij Rasterdruk, Amsterdam Institut voor Grafische Techniek (1945).*
3. *Morse, S., Durelli, A.J. and Sciammarella, C.A., J. Eng. Mech. Div., Proc. ASCE,* **86** *(EM-4), 105-126 (1960).*
4. *Theocaris, P., Moiré Fringes in Strain Analysis, Pergamon Press, New York (1969).*
5. *Durelli, A.J. and Parks, V.J., Moiré Analysis of Strain, Prentice Hall, Englewood Cliffs, NJ (1970).*

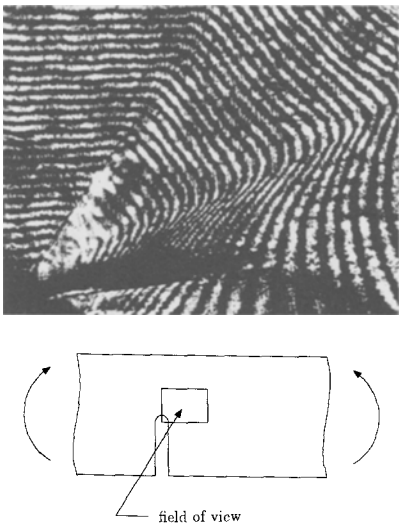

(a)

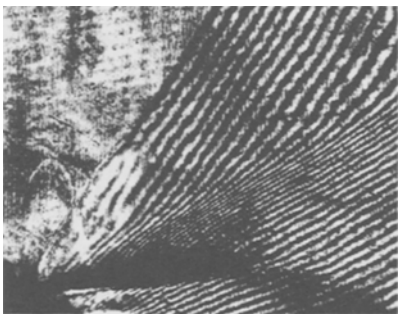

(b)

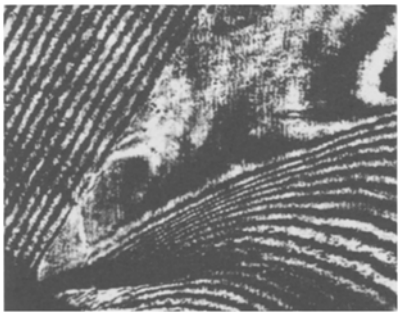

(c)

Fig. 10—(a) Fringes near the crack tip for **g** chosen to show fringe kinks; (b) fringes with **g** chosen to null central fan; (c) fringes with **g** chosen to null side fan

6. Parks, V.J., *Handbook on Experimental Mechanics*, ed. A.S. Kobayashi, Prentice Hall, Englewood Cliffs, NJ, Chapt. 6 (1987).
7. Chiang, F.P., *Manual on Experimental Stress Analysis*, ed. J.F. Doyle, SEM, Bethel, CT, Chapt. 7 (1989).
8. Guild, J., *The Interference System of Crossed Diffraction Gratings*, Clarendon Press, Oxford (1956).
9. Post, D., *Handbook on Experimental Mechanics*, ed. A.S. Kobayashi, Prentice Hall, Englewood Cliffs, NJ, Chapt. 7 (1987).
10. McKelvie, J., "Experimental Photomechanics: Fundamental Physics and Mathematical Contrivances," MicroMechanics: Experimental Techniques, Proc. Symp. on Experimental Techniques, ASME 1989 Winter Annual Mtg., AMD-102, ed. W.N. Sharpe, Jr. (1989).
11. Shield, T.W. and Kim, K.-S., "An Experimental Study of the Plastic Deformation Fields near a Crack Tip in an Iron-Silicon Single Crystal," submitted to J. Mech. and Phys. of Solids (1990).
12. Born, M. and Wolf, E., *Principles of Optics*, 3rd Ed., Pergamon Press (1965).
13. Shield, T.W., Kim, K.-S. and Nikolic, R., "Moiré Microscope for the Experimental Determination of the In-Plane Displacement Field Near a Crack Tip in a Single Crystal," MicroMechanics: Experimental Techniques, Proc. Symp. on Experimental Techniques, ASME 1989 Winter Annual Mtg., AMD-102, ed. W.N. Sharpe, Jr. (1989).

Appendix A

Diffraction on a Deformed Grating

Diffraction on a deformed grating is depicted in Fig. 11. The incident light beam is represented by eq (1). If transfer (transmittivity or reflectivity) function of the deformed grating, T, is considered as a periodic function of $\mathbf{X}^*$ but not an explicit function of $\mathbf{F}(\mathbf{X}^*)$, then T can be represented as a Fourier series in $\mathbf{X}^*$ space,

$$T(\mathbf{x}^*) = \sum_{N=-\infty}^{\infty} t_N e^{iN\Phi\{x^*(x^*)\}} \qquad \text{(A1)}$$

Therefore, the boundary condition right after the light goes through the deformed grating is expressed as

$$\mathbf{E}(\mathbf{x}^{*+},t) = \sum_{N=-\infty}^{\infty} t_N \mathbf{A} e^{i[\psi(x^*,t)+N\Phi\{x^*(x^*)\}]} \qquad \text{(A2)}$$

With this boundary condition, the high spatial frequency field above the cut off frequency, $|\mathbf{k}|$, decays exponentially from the boundary and only finite number of diffraction order survives at far field. For the surviving Nth order diffraction field, the electric field can be expressed in eq (3), satisfying the boundary condition given as the Nth term in the series of eq (A2). This shows that the surviving far-field, Fraunhoffer diffraction field, has the phase relation as given in eq (4).

Error estimation for moiré interferometry is out of the scope of this paper. However, the following comments will be noted. Dynamic range, on $\mathbf{F}$, of the moiré method due to aperture size can be easily assessed with eq (9). The Rayleigh criterion[12] enters into eq (5) for the uncertainty of the phase due to the finite-size area of the grating participating in the diffraction process and moiré-fringe formation. The phase variation represented as the left-hand side of eq (6) should be bound by the diffraction limit. Nevertheless the most serious error sources in moiré interferometry are the original quality of the grating and the change of the grating quality caused by surface deformation. If the original quality of the grating is poor, the Fourier series representation of the grating in eq (A1) is no longer accurate. If the grating quality changes with the surface deformation, then the transfer function, T, is not only a function of $\mathbf{X}^*$ but also a time-history functional of $\mathbf{F}$. If we consider a monotonic deformation path for the grating deformation, T can be represented as a function of $\mathbf{X}^*$ and $\mathbf{F}$, say, $T(\mathbf{X}^*,\mathbf{F})$. Assuming T is analytic with respect to $\mathbf{F}$, it can be expanded as

$$T(\mathbf{X}^*,\mathbf{F}) = T(\mathbf{X}^*,\mathbf{I}) + \frac{\partial T(\mathbf{X}^*,\mathbf{I})}{\partial \mathbf{F}} : (\mathbf{F}-\mathbf{I}) + \ldots . \qquad \text{(A3)}$$

The first term in eq (A3) can be expressed as eq (A1). However, the transfer function, T, has extra terms in eq (A3), which cause extra phase contribution in $\tilde{\psi}_N(\mathbf{x}^*,t)$. The extra phase contribution can be taken into account in the expression of $\Phi\{\mathbf{x}^*,\mathbf{F}(\mathbf{x}^*)\}$, and then the reciprocal grating vector in eq (18) should be replaced by $\frac{1}{2\pi}\nabla_{x^*}\Phi$, where

$$\nabla_{x^*}\Phi = 2\pi\mathbf{G}^* + \frac{\partial \Phi}{\partial \mathbf{F}} : (\nabla_{x^*}\mathbf{F}) \cdot \mathbf{F} \qquad \text{(A4)}$$

As shown in this equation, if the deformation is uniform, i.e., $\nabla_{x^*}\mathbf{F} = 0$, then such an error disappears. If the deformation is highly inhomogeneous and the deformation is large, such an error may not be negligible.

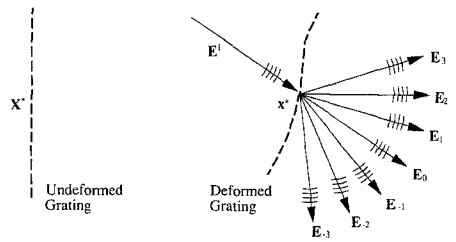

Fig. 11—Diffraction on a deformed grating

Appendix B

Specimen Specifications

The single crystal of Fe-Si considered here has dimensions of 7.45 mm × 6.00 mm × 26.05 mm. This bar was extended to the length of 51.95 mm by welding 12.95-mm long polycrystalline bars of the same cross section to each end. Then a crack-like single-edge notch was introduced at the center of the crystal to a depth of 2.05 mm and a width of 200 μm. The prospective crack-propagation direction is [100] the crack plane is (011), and the crack front is aligned in the [01 $\bar{1}$] direction.

The specimen was loaded in a four-point bending fixture by an Instron machine in displacement control. The inner span of the loading points on the unnotched face of the specimen was 20 mm, and the outer span on the notched side was 30 mm. All the moiré pictures reported in this paper correspond to the deformed configuration after final unloading.

A grid made up of two orthogonal gratings with 5-μm spacing was photo-lithographically deposited on the polished specimen surface. The Plate Impact Laboratory at Brown University used a Ronchi ruled grating and a double-exposure contact print to produce this grid. 'Kodak Thin Film Resist' (KTFR) photo resist was spin coated onto the specimen surface. An ultravoilet lamp was used for the exposures because KTFR has maximum sensitivity at a wavelength of 400 nm.